Vibration and Aerodynamic Characteristics of Dielectric Elastomer Membranes of Various Shapes

Pratik Sarker *, Bianca Fernandez, M. Shafiqur Rahman

Posted Date: 23 March 2026

doi: 10.20944/preprints202603.1712.v1

Keywords: aerodynamics; finite element; fluid-structure interaction; vibration; membrane; dielectric elastomer

 doi:10.20944/preprints202603.1712.v1

Article

Vibration and Aerodynamic Characteristics of Dielectric Elastomer Membranes of Various Shapes

Pratik Sarker [1,*], Bianca Fernandez [1] and M. Shafiqur Rahman [2]

[1] Embry-Riddle Aeronautical University, Prescott, Arizona, USA

[2] Louisiana Tech University, Ruston, Louisiana, USA

* Correspondence: sarkerp@erau.edu; Tel.: +1-928-777-3810

Abstract

The dielectric elastomer is a category of electroactive polymer capable of having large deformation under electric excitation and vice versa. They show great potential for proper maneuvering of small-scale aerial vehicles due to low density and fast actuation, and the successful design demands proper prediction of their overall dynamic characteristics. However, these characteristics cannot be accurately predicted from lower-order material approximation and/or one specific elastomer shape under a specific flow velocity, pretension, and relaxation. In this research, a comprehensive modal and aerodynamic analysis for VHB 4910 dielectric elastomer membrane of three different shapes are computationally investigated under different electric excitations, pretensions, and flow velocities using higher-order Ogden model. A finite element model and a two-way, fully coupled, fluid-structure interaction model are developed to obtain vibration and aerodynamic characteristics, respectively, for different membrane shapes. It is found that the variation of electric excitation, pretension, and air velocity is influential to alter the overall dynamics of the membrane and is unique to specific shapes. The rectangular membrane shows higher vibration frequency for the fundamental mode whereas the circular membrane provides higher frequencies in higher modes. Increased relaxation for a membrane prestretch higher than the moderate range of stretch ratio ($\lambda = 3$) demonstrates slight increase in lift coefficient within a small range of angle of attack followed by a decrease after exceeding that range. Both the rectangular and elliptical membranes show more flexibility to delay the stall compared to the circular membrane. The circular membrane is observed to have more potential for enhancing the aerodynamic performance and altering the flow field within a certain range of electric excitation and pretension. Computational results are compared with published experimental results to validate the corresponding models.

Keywords: aerodynamics; finite element; fluid-structure interaction; vibration; membrane; dielectric elastomer

1. Introduction

Among various types of smart materials, dielectric elastomers (DEs) fall into the category of electroactive polymers which can change their shapes in response to applied electric excitation. Conversely, when subjected to electric stimulation, DEs react to providing mechanical deformation. This built-in electromechanical characteristics of DEs have made them unique for various applications including energy conversion, artificial anatomical systems, control of small-scale aerial structures, actuation of mechanisms, shape memory alloys, artificial/biological insect wings, and many more [1–4]. For such an application regarding small aerial structures, in majority of cases, the surrounding aerodynamic environment is unpredictable, requiring proper control of maneuverability. The small size of the vehicles makes packaging separate control mechanisms challenging, resulting in lower aerodynamic performance. To assist this challenge, DEs are found to be promising for rapid adaptation to changes in environmental conditions due to their unique electromechanical characteristics. The deformation of the aerial structures composed of DEs due to

 doi:10.20944/preprints202603.1712.v1

aerodynamic loading and the deformation of the surrounding fluid domain due to the change in shape of the structure affect each other resulting in the change of overall aeroelastic characteristics [5,6]. Hence, comprehensive understanding of the coupled interaction between the flexible structure and the aerodynamic environment is crucial to explore the associated dynamic behavior of DEs for the robust and reliable design of small-scale aerial structures with enhanced safety and agility.

To explore the characteristics of DE materials under dynamic loading deeply, proper identification of important parameters that can play a significant role in influencing the mutual interaction between the structure and the aerodynamic environment is necessary. Membrane pretension is one such parameter which affects both the vibration and aerodynamic characteristics of the pliant structure and needs to be regulated precisely for specific applications. The pretension can be altered by changing the stretch ratio and from the relaxation induced by electric excitation [7,8]. In general, for pliant DE membranes, the plane stress condition is considered [7] to evaluate the net stress state of the membrane in presence of both pretension and electric excitation. Usually, the ideal aerodynamic environment considered for small-scale aerial structures is associated with low Reynolds number (Re) [9] flow which, in combination with an electric voltage influences the overall aerodynamic efficiency of such structures [5]. The material of the pliant wing needs to be carefully considered for effective lift generation and power consumption and requires sufficient flexibility to enhance aerodynamic efficiency with proper regulation. Lang et al. [10] experimentally investigated the aerodynamic characteristics of flapping wings composed of different materials and found that lift can be improved for wings composed of higher elastic modulus, however, at the cost of increased power.

In search of suitable DE materials to use for pliant wing structures, VHB 4910 membrane is proposed by several researchers [4,5,11,12] due to its properties well aligned with the flexible nature of pliant wings. However, reliability of a selected material model to accurately reflect the dynamic characteristics of the VHB 4910 membrane depends on the types of experiments used to obtain the corresponding properties. VHB 4910 material characteristics can be captured with reasonable accuracy by comparing its behavior to a hyperelastic material [13–15] due to its capability of undergoing large strain. However, the use of lower-order models often cannot predict the dynamic characteristics of the membrane properly, especially if the pretension is relatively high. The simplest but a lower-order model is the Neo-Hookean hyperelastic model [13] which is unable to predict the large-strain behavior of the membrane with reasonable accuracy when the strain ranges more than 20%. An alternative and more accurate model is the higher order Ogden model [14,16] for large strain applications which is versatile and at the same time, a good fit to use with relevant constitutive relationships for hyperelastic materials. One of the greatest benefits of modeling the dynamics of DE membrane using the Ogden model [14] is that it can handle the strain as large as 700% to predict results with reasonable accuracy. With the use of Ogden model, DE membrane behavior can be approximated closely by treating it as an incompressible material and ignoring the effect of viscoelasticity [17].

When correlated with wind-tunnel experiments [6,18], computational simulation of vibration and aerodynamic behavior of a pliant wing can be of significant advantage to provide wider range of data and establish useful relationships between the governing parameters, which could be effective for successful design and control of small aerial vehicles. Pulok et al. [6] investigated the modal and aerodynamic characteristics of a circular DE membrane for different Re by conducting vibration and wind-tunnel tests, however, the latter did not consider the effect of electric excitation. This left a gap to properly predict the actual dynamic behavior of the membrane in presence of electric excitation which is important for proper regulation of structures composed of DE materials in a certain aerodynamic environment. This demands the necessity of conducting robust, two-way, coupled fluid-structure interaction (FSI) [9,19,20] simulations which can lead to comprehensive understanding of the mechanism of interaction between the structure and the fluid. Genç et al. [21] conducted an experimental study on FSI analysis for flexible membrane wings over a range of angles of attack (AoAs) for various Re. They noticed that for flexible wings with higher aspect ratio, higher

 doi:10.20944/preprints202603.1712.v1

vibration modes were characterized and as the Re and aspect ratio increased, the maximum deformation of the membrane also increased. Liang et al. [22] investigated the dynamic behavior of a hollow fiber membrane for different lengths and air velocities by developing a two-way FSI model and analyzed the relevant flow characteristics under air-induced condition. They verified the numerical study by experiments and found that the natural frequencies of the membrane were more sensitive to change in length of the membrane compared to the change in air velocities. These studies indicate that a successful FSI analysis can provide valuable insight in proper prediction of the dynamic behavior of pliant wings.

The aeroelastic characteristics of the wing material play an important role in determining the overall performance of the wing structure subjected to fluid flows, especially if the wing structure is pliant [5,23,24]. The maneuverability and stability of the wing structure can be influenced to a greater extent if the aeroelastic properties of the pliant wing are tunable. Yeh and Chiang [25] developed a bat-inspired, two degrees-of-freedom (DOFs) flapping mechanism capable of capturing fundamental wing folding motions to investigate the effect of wing elasticity on aerodynamics. They fabricated polydimethylsiloxane membranes by properly adjusting the ratio of the curing agent exhibiting the greatest extensibility and the lowest Young's modulus in their study. This ensured reliable motion transmission and allowed systematic investigation of wing flexibility regarding the aerodynamic performance.

Majority of the existing studies conducted so far regarding the investigation of dynamic characteristics of DE wing structures either involve one specific shape and/or without any electric excitation, have evaluated the membrane dynamics subjected to only one velocity under a single pretension, or have used a lower-order model. This motivated the authors to explore the dynamics of DE membranes further for different variations of parameters. Therefore, in this study, a comprehensive dynamic analysis of three different shapes of DE membranes subjected to different air flow velocities, electric excitations, and pretensions is performed in terms of vibration characteristic, aerodynamic behavior, and aeroelastic nature through computational simulations using a higher-order model. A finite element (FE) analysis is performed to evaluate the modal characteristics of DE membranes subjected to mechanical pretension and electric excitation. For the aerodynamic and aeroelastic analysis, a two-way, fully coupled FSI simulation is conducted for three shapes of the membranes under varying air flow velocities, electric excitation, and membrane pretension. Computational results are compared with experimental results published in literature to validate the FE and FSI models and the convergence study is also performed to demonstrate the mesh independence of the computational model.

2. Materials and Methods

In this analysis, VHB 4910 [4,5,11,12] DE membranes are used to obtain their vibration, aerodynamic, and aeroelastic characteristics from computational simulation. Three different shapes of DE membranes−rectangular, elliptical, and circular shapes are considered as shown in Figure 1. Each of the VHB 4910 membrane has an initial thickness of 1 mm [6,26,27] before pretension and maintains same surface area under all pretension conditions. The pretension is applied to the membrane by stretching it biaxially maintaining a uniform stretch ratio λ, defined specifically as λ_1 and λ_2 along in-plane X and Y directions, respectively, as shown in Figure 1. The Z axis is defined as normal to the membrane surface and the stretch ratio in that direction is specified as λ_3.

 doi:10.20944/preprints202603.1712.v1

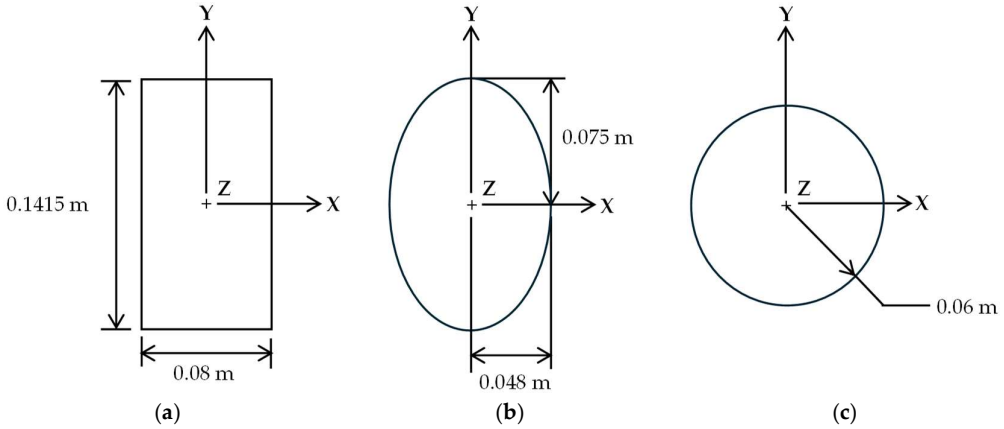

Figure 1. Different geometric shapes of VHB 4910 membranes, **(a)** rectangle; **(b)** ellipse; **(c)** circle.

For the vibration analysis, an FE model is developed in the commercially available software package, COMSOL Multiphysics, version 6.2, which is solved for obtaining the natural frequencies of free vibration for the first four modes of the prestressed membranes of various shapes under different electric excitations. For the aerodynamic and aeroelastic analysis, the fully coupled FSI model is developed in COMSOL Multiphysics which is solved for lift and drag coefficients, aerodynamic efficiency, and aerodynamic load-induced deformations of the membranes for different fluid flow velocities, electric excitations and stretch ratios.

2.1. Material Model for DE Membranes

Due to the capability of undergoing large strains, the DE membrane is modeled by. using a hyperelastic material model [13–15]. The Ogden hyperelastic model [14–16] is used for both vibration, aerodynamic and aeroelastic analysis to overcome the limitation of the Neo-Hookean hyperelastic model [6,13] which is based only on the uniaxial tension test data. The strain energy density function W for the Ogden [14–16] hyperelastic material model is defined as,

$$W = \sum_{i=1}^{N} \frac{\mu_i}{\alpha_i}\left(\lambda_1^{\alpha_i} + \lambda_2^{\alpha_i} + \lambda_3^{\alpha_i} - 3\right) \quad (1)$$

where λ_1, λ_2, and λ_3 are stretch ratios along X, Y, and Z directions, respectively, with reference to Figure 1, and μ_i and α_i are the material constants determined empirically from uniaxial and constrained tension test for the Ogden model. Nearly incompressible behavior is considered for the VHB 4910 membrane defined by the Ogden model in the FE and FSI models and the effect of viscoelasticity is ignored. The shear modulus of the membrane, μ_s defined by the Ogden model, is represented by the following equation:

$$2\mu_s = \sum_{i=1}^{N} \mu_i \alpha_i \quad (2)$$

In Equation (2), when $i = 1$ and $\alpha_1 = 2$, it recovers the simplest Neo-Hookean model [6,14]. When electric excitation is applied on the membrane in addition to mechanical stretch, the membrane undergoes relaxation, a softening effect induced from the compressive stress generated by the electric excitation, also known as the Maxwell stress [26]. In the reported experimental studies, electric excitation can be implemented by using conductive electrodes on upper and lower surfaces of the membrane in the form of carbon grease [5,28]. The net stresses on the membrane, σ_x and σ_y in X and Y directions, respectively, are combinations of the tensile stress from mechanical pretension and compressive Maxwell stress from electric excitation and are estimated from Equations (3) and (4) [7]:

$$\sigma_x = \mu_s\left({\lambda_1}^2 - {\lambda_1}^{-2}{\lambda_2}^{-2}\right) - \varepsilon E^2 \quad (3)$$

$$\sigma_y = \mu_s\left({\lambda_2}^2 - {\lambda_2}^{-2}{\lambda_1}^{-2}\right) - \varepsilon E^2 \quad (4)$$

where ε is the permittivity and E is the true electric field defined as the ratio of the electric voltage and the thickness of the membrane after the pretension is applied. The thickness of the membrane

 doi:10.20944/preprints202603.1712.v1

after the pretension can be expressed as $t_u/(\lambda_1\lambda_2)$ [7] where t_u is the thickness of the membrane in the undeformed state. The parameters of the Ogden hyperelastic model mentioned in Equation (2) are listed in Table 1 [29]. Table 2 represents the numerical values of σ_x and σ_y for stretch ratios 2, 3, 4.5, and 4.9 for electric excitations of 0 kV, 3.6 kV, and 4.5 kV for $\varepsilon = 4.02866\times10^{-11}$ F/m; and Table 3 lists the physical properties of the VHB 4910 membrane [6] considered in this analysis.

Table 1. Ogden model parameters [29] for the VHB 4910 DE membrane.

Parameters of the Ogden Model		
$\mu_1 = 54.8\text{e}3$ Pa	$\mu_2 = 910$ Pa	$\mu_3 = -6.30$ Pa
$\alpha_1 = 0.70$	$\alpha_2 = 3.25$	$\alpha_3 = -3.70$

Table 2. Membrane stresses at different voltages based on the Ogden model.

Stretch ratio	**Voltage, kV**	**σ_x, Pa**	**σ_y, Pa**
$\lambda_1 = 2$ $\lambda_2 = 2$	0	8.15e4	8.15e4
	3.6	7.31e4	7.31e4
	4.5	6.84e4	6.84e4
$\lambda_1 = 3$ $\lambda_2 = 3$	0	1.86e5	1.86e5
	3.6	1.43e5	1.43e5
	4.5	1.99e5	1.99e5
$\lambda_1 = 4.5$ $\lambda_2 = 4.5$	0	4.19e5	4.19e5
	3.6	2.05e5	2.05e5
	4.5	8.45e4	8.45e4
$\lambda_1 = 4.9$ $\lambda_2 = 4.9$	0	4.97e5	4.97e5
	3.6	1.96e5	1.96e5
	4.5	2.66e4	2.66e4

Table 3. Properties of the VHB 4910 DE membrane.

Properties	
Density	1411.03 kg/m^3
Modulus of Elasticity	139,800 Pa
Poisson's Ratio	0.499

2.2. Vibration Analysis

A computational 3D FE model of free vibration for each shape of the membrane in COMSOL Multiphysics 6.2 is developed by using the eigenfrequency solver from the structural mechanics module. Each shape of the membrane is modeled as a 3D pliant structure with the appropriate stress values mentioned in Table 2 for various electric excitations given by Equations (3) and (4) based on the Ogden model. The nonlinear geometry effect is considered to solve the FE model of vibration for the first four modes. For all shapes of the membranes, fixed boundary conditions (BCs) are used in the membrane edges as listed in Table 4 below.

Table 4. Boundary conditions for the FE model of vibration of VHB 4910 membranes.

Boundary Conditions					
d_x	d_y	d_z	θ_x	θ_y	θ_z
0	0	0	0	0	0

 doi:10.20944/preprints202603.1712.v1

In Table 4, d_x, d_y, and d_z represent the linear displacements of the membrane along the X, Y, and Z axes, respectively, and θ_x, θ_y, and θ_z are the rotational displacements about the X, Y, and Z axes, respectively; with reference to Figure 1.

2.3. Aerodynamic and Aeroelastic Analysis

2.3.1. Development of the Fluid-Structure Interaction Model

For the aerodynamic and aeroelastic analysis, a two-way, fully coupled, 3D FSI model is developed in COMSOL Multiphysics, version 6.2, composed of the solid DE membrane used as the structural FE model; and the air surrounding the membrane, used as the computational fluid dynamics (CFD) model [30]. Both the FE and the CFD domains are described in Figure 2 with the FE domain embedded into the CFD domain. Three different air flow velocities, 5 m/s, 10 m/s, and 13.4 m/s are used as the input velocities for the membrane corresponding to low-Re condition [31], suitable for small scale-aerial structures. For all the membrane shapes, the 3D air domain has a length, width, and height of 7 m, 5 m, and 5 m, respectively, where the largest dimension is aligned with the flow direction along the X axis. It is to note that the fluid domain size is chosen to be large enough compared to the solid membrane to capture the proper flow physics [32]. Due to the low-Re condition, a laminar flow model is considered. The Re is calculated based on the characteristic length of each geometric shape of the membrane as $\mathrm{Re} = \rho_a V L_c/\mu_d$, where L_c is the characteristic length of the membrane aligned parallel to the airflow velocity, V is the air flow velocity, ρ_a is the density of air, and μ_d is the dynamic viscosity of air.

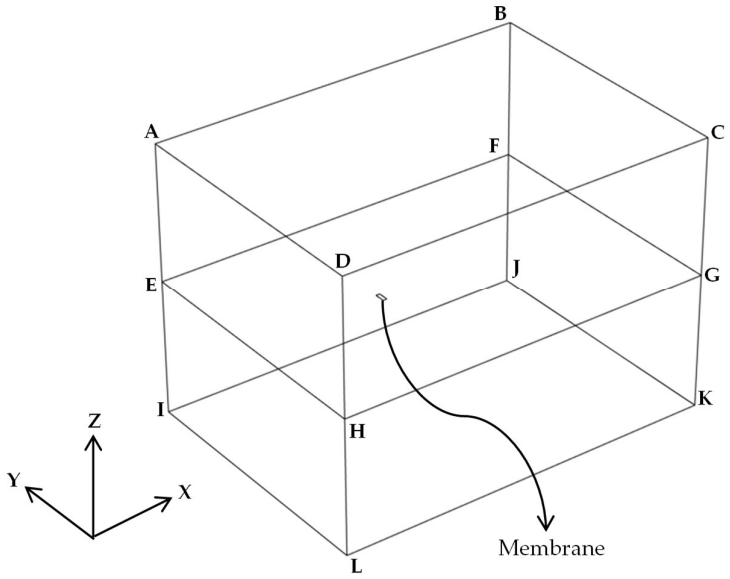

Figure 2. The air domain enclosing the membrane in the fluid-structure interaction model.

Figure 3 shows the 2D orientation of the DE membrane in the fluid domain with the direction of V related to the AoA, α_a. The physical properties of air constituting the CFD domain are listed in Table 5 by considering atmospheric condition surrounding the membrane [6].

 doi:10.20944/preprints202603.1712.v1

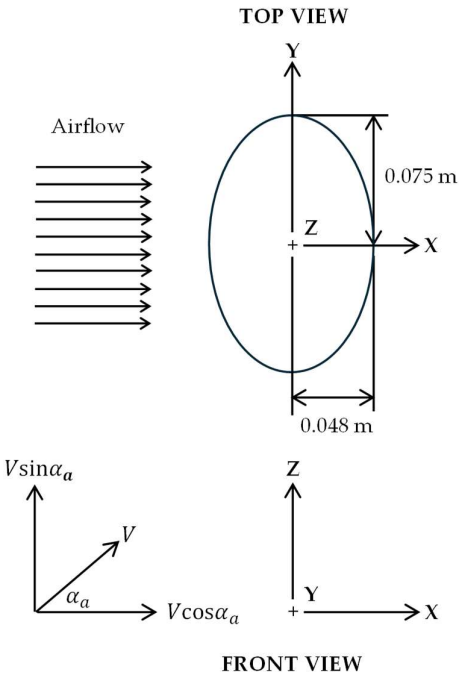

Figure 3. Direction of airflow velocity over the membrane.

Table 5. Properties of the air domain.

Properties	
Density	1.226 kg/m^3
Dynamic viscosity	1.81e-5 Pas

2.3.2. Boundary Conditions

The BCs are assigned appropriately for both the FE and the CFD domain. For the FE model of the solid membrane enclosed by the CFD domain, same BCs listed in Table 4 are used. For the CFD model, both velocity and pressure BCs are applied according to the flow physics corresponding to the external flow over the membrane and are listed in Table 6. In Table 6, u, v, and w represent the velocity components of air along the X, Y, and Z directions respectively, in relation to Figures 2 and 3. The inlet BC is assigned as a velocity BC normal to the ADHLIEA plane in Figure 2 and pressure BC is assigned in the downstream direction of the flow for the plane BCGKJFB of the CFD domain. The side BCs are assigned by considering the CFD domain far enough from the enclosed membrane and hence, the velocities along the side boundaries of the CFD domain are considered unaffected by the fluid-solid interaction. Therefore, the inlet BCs are also used as the side BCs for the CFD domain surfaces parallel to XY and XZ planes as shown in Figure 2 and listed in Table 6. For the inner wall, which is the membrane surface at the mid-plane of the CFD domain parallel to XY plane in Figure 2, the no-slip BC is applied.

Table 6. Boundary conditions for the fluid domain.

Boundary Conditions					
		Velocity, m/s			Pressure, Pa
Name	Parameter	u	v	w	P
Inlet (ADHLIEA)	Velocity	$V\cos\alpha_a$	0	$V\sin\alpha_a$	-
Outlet (BCGKJFB)	Pressure	-	-	-	0

 doi:10.20944/preprints202603.1712.v1

Side 1 (ABCDA)	Velocity	$V\cos\alpha_a$	0	$V\sin\alpha_a$	-
Side 2 (IJKLI)	Velocity	$V\cos\alpha_a$	0	$V\sin\alpha_a$	
Side 3 (DCGKLHD)	Velocity	$V\cos\alpha_a$	0	$V\sin\alpha_a$	
Side 4 (ABFJIEA)	Velocity	$V\cos\alpha_a$	0	$V\sin\alpha_a$	
Inner wall (membrane surface)	Velocity	0	0	0	-

2.3.3. Mesh Formation

To mesh the computational model of the membrane for both vibration and aerodynamic analysis, similar meshing technique is used. For the FE model of vibration of the membrane, user-controlled mesh configuration is used in COMSOL Multiphysics. 2D, free triangular elements are used for meshing the membrane domain due to their versatility and capability of handling curved geometry, with the maximum element size of 0.004 m. Figure 4 shows the meshed FE domain of the circular membrane.

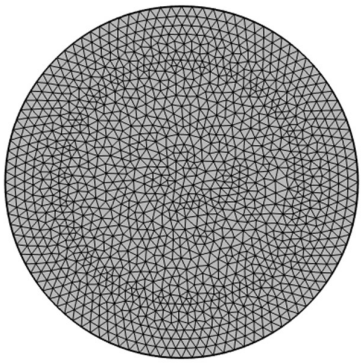

Figure 4. The converged mesh of the circular membrane (solid domain).

For the FSI analysis, user-controlled mesh is used again for the entire domain combining the FE and CFD domain which is calibrated for fluid dynamics. Aside from the aforementioned meshing technique of the FE domain comprising the membrane, the maximum element size considered for the free triangular element for the CFD domain is 0.2 m and the minimum element size was 0.003 m. The maximum element growth rate considered is 1.05 to ensure a gradual transition from the smallest to the largest element in the entire domain. After using the free triangular elements in the mid-plane of the CFD domain (EFGHE plane in Figure 2), the 2D surface mesh was swept through the entire CFD domain and distributed symmetrically with respect to the mid-plane maintaining an element ratio of 200. The number of boundary layers for the FSI analysis is determined by the automatic mesh algorithm. The meshed CFD domain in its finest element size is depicted in Figure 5.

 doi:10.20944/preprints202603.1712.v1

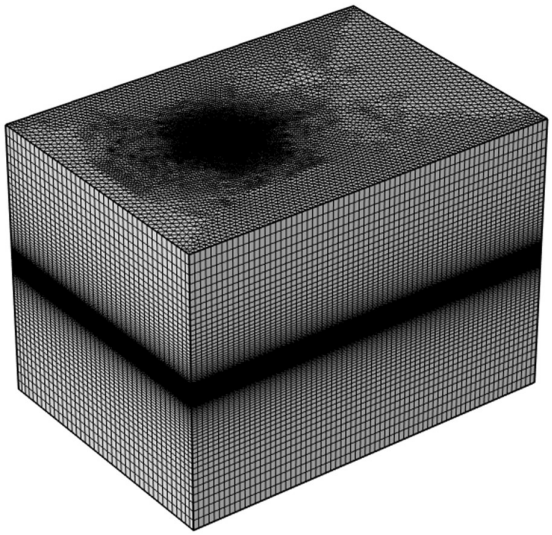

Figure 5. The converged mesh of the air (fluid) domain.

2.4. Governing Equations for the Computational FSI Model

The FSI model couples the fluid domain with the solid domain where the fluid is represented by the air and the solid domain is represented by the membrane submerged within the air. The corresponding governing equations for the computational model are discussed in the subsequent sections.

2.4.1. Solid Domain

The solid membrane domain is governed by Newton's second law as below [22]:

$$\rho_m \mathbf{a_s} = \nabla . \boldsymbol{\sigma_s} + \mathbf{f_s} \quad (5)$$

where ρ_m is the density of the membrane, $\mathbf{a_s}$ is the acceleration vector, $\boldsymbol{\sigma_s}$ is the stress tensor, and $\mathbf{f_s}$ is the force vector per unit volume.

2.4.2. Fluid Domain

For the fluid domain, the air is considered as an incompressible, Newtonian fluid and corresponding field variables of the air domain are associated with the continuity equation and the momentum equations given by Equations (6) and (7), respectively, as below:

$$\frac{\partial u}{\partial x} + \frac{\partial v}{\partial y} + \frac{\partial w}{\partial z} = 0 \quad (6)$$

$$\rho_a \left(\frac{\partial u}{\partial t} + u\frac{\partial u}{\partial x} + v\frac{\partial u}{\partial y} + w\frac{\partial u}{\partial z} \right) = -\frac{\partial P}{\partial x} + \rho_a g_x + \mu_d \left(\frac{\partial^2 u}{\partial x^2} + \frac{\partial^2 u}{\partial y^2} + \frac{\partial^2 u}{\partial z^2} \right) \quad (7a)$$

$$\rho_a \left(\frac{\partial v}{\partial t} + u\frac{\partial v}{\partial x} + v\frac{\partial v}{\partial y} + w\frac{\partial v}{\partial z} \right) = -\frac{\partial P}{\partial y} + \rho_a g_y + \mu_d \left(\frac{\partial^2 v}{\partial x^2} + \frac{\partial^2 v}{\partial y^2} + \frac{\partial^2 v}{\partial z^2} \right) \quad (7b)$$

$$\rho_a \left(\frac{\partial w}{\partial t} + u\frac{\partial w}{\partial x} + v\frac{\partial w}{\partial y} + w\frac{\partial w}{\partial z} \right) = -\frac{\partial P}{\partial z} + \rho_a g_z + \mu_d \left(\frac{\partial^2 w}{\partial x^2} + \frac{\partial^2 w}{\partial y^2} + \frac{\partial^2 w}{\partial z^2} \right) \quad (7c)$$

where x, y, and z are independent displacement variables along the global X, Y, and Z directions, respectively; u, v, and w are velocity components of air along X, Y, and Z directions, respectively; t is time, P is pressure; and g_x, g_y, and g_z are the accelerations due to gravity along X, Y, and Z directions, respectively.

2.5. Experimental Research from Literature

2.5.1. Vibration Testing Setup

 doi:10.20944/preprints202603.1712.v1

According to the literature survey, some experimental studies are conducted to investigate the structural dynamics of flexible membranes of specific geometric shapes. For the free vibration analysis, the experimental setup used by Pulok and Chakravarty [6] is described in Figure 6. They used a closed loop vibration testing system composed of a Data Physics GW-V20 PA 100E SignalForce shaker which induced a suitable vibratory force to the membrane contained by a rigid frame securely attached to the top of the vibrating shaker head. The shaker is used together with the ABAQUS Vibration Controller from Data Physics, a Data Physics signal amplifier, and a Dytran Instruments accelerometer with a precision of sensing 19.69 mV/g. The electric excitation on the membrane is applied by a separate transformer capable of providing high voltage with low current. A digital image correlation system composed of two high-speed cameras from Photron along with the relevant data acquisition system are utilized to capture the images of the vibrating membrane. These images are processed further to measure the out-of-plane displacements using the VIC-3D software and ultimately, the vibration frequencies were obtained from Fast Fourier Transform of the membrane displacements.

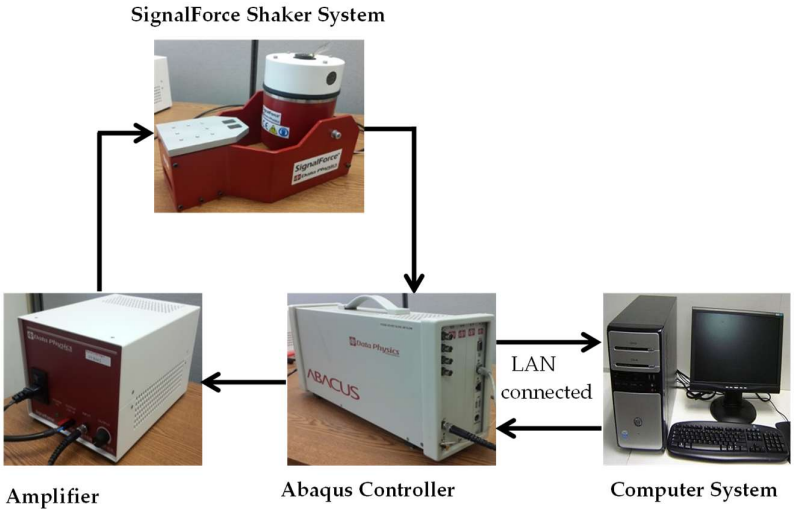

Figure 6. Experimental setup for free vibration analysis of the membrane.

2.5.2. Wind-Tunnel Experimental Research

A wind-tunnel experiment was conducted by [6] where they investigated the dynamic performance of the circular membrane under aerodynamic loading. A schematic of such a wind-tunnel is described in Figure 7 composed of a variable-speed fan drawing air into the wind tunnel. To ensure the characteristics of laminar airflow through the test section, a honeycomb flow straightener is used in the wind-tunnel. A detailed internal view of the test section of the wind tunnel including the model positioning system and pistol-grip sting balance is depicted in Figure 7. The purpose of using the sting balance and the model positioning system is to evaluate the aerodynamic forces on the membrane and to regulate the AoA, respectively. It is to note that the effect of electric excitation on the aerodynamic performance of the DE membrane was not studied by [6] in their wind-tunnel experiment due to some limitations in the system restricting the high voltage application inside the test section. This limitation of the wind tunnel in conducting such experiments is also one of the inspirations for the authors to explore the membrane dynamics further by conducting a robust, two-way, fully coupled FSI simulation.

 doi:10.20944/preprints202603.1712.v1

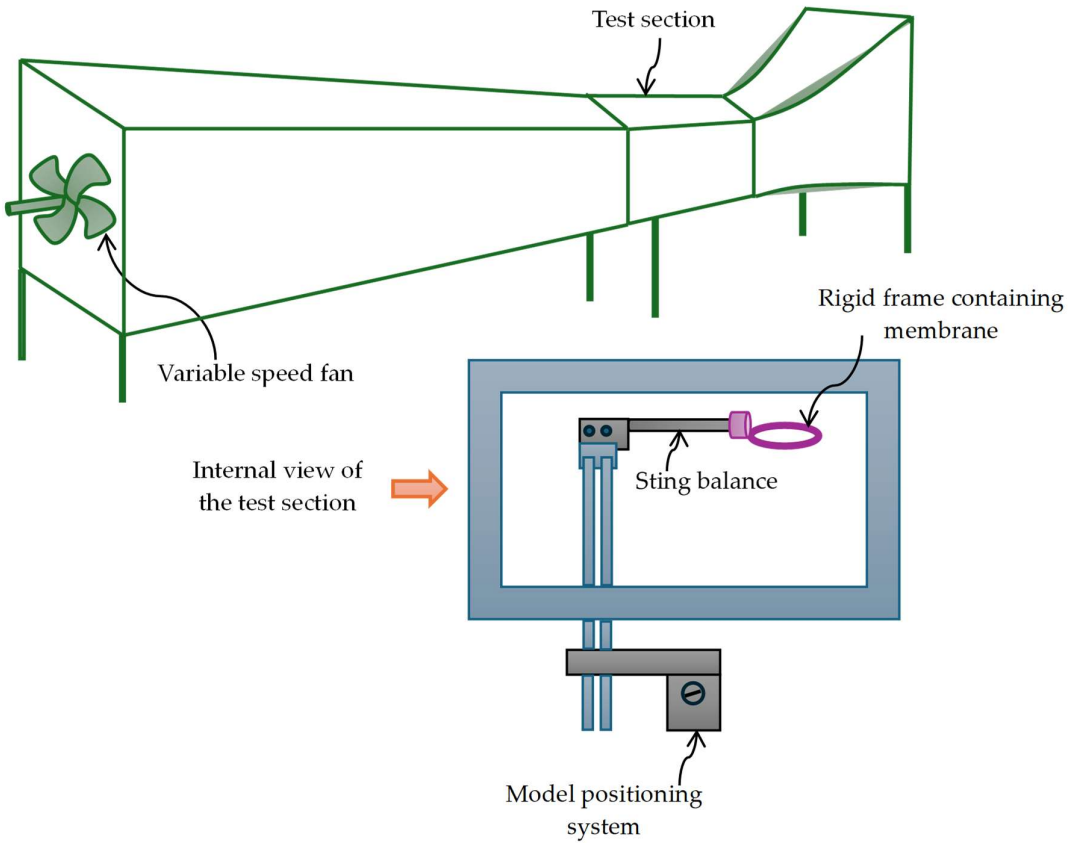

Figure 7. A schematic of the wind-tunnel system used by Pulok and Chakravarty [6] in their experimental study including the model positing system and the sting balance.

3. Model Validation

3.1. Experimental Validation of the Finite Element Model

To validate the FE model of free vibration analysis, the computational results are compared with the experimental results. Figure 8(a) shows a comparison of the fundamental natural frequencies (first mode frequency) of free vibration of an elliptical DE membrane obtained from the FE analysis and that from the experimental research conducted by Hays et al. [28] for 0 kV electric excitation and stretch ratio of 3. The elliptical DE membrane has 1 mm initial thickness having a semi-major axis of 0.1 m and a semi-minor axis of 0.05 m where the membrane was secured within a rigid frame maintaining a fixed (BC) at the edge. From Figure 8(a), the FE frequency based on the Ogden model closely approximates the experimental finding maintaining a percentage deviation of 3.74% and thereby justifying that the computational FE model of vibration provides results with reasonable accuracy.

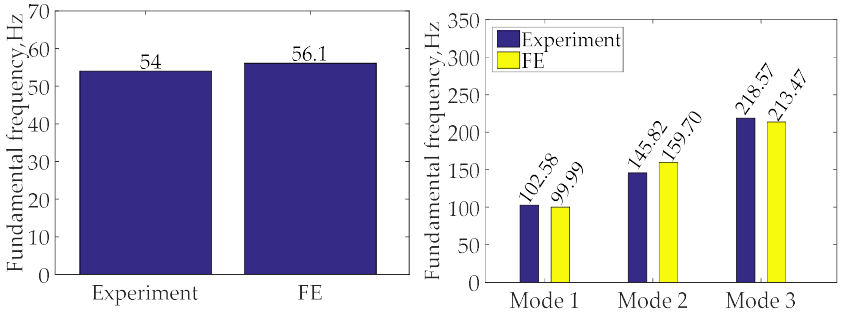

 doi:10.20944/preprints202603.1712.v1

Figure 8. Comparison of the natural frequency obtained from experiment and from finite element analysis for **(a)** elliptical DE membrane with $\lambda = 3$ and 0 kV electric excitation; **(b)** circular DE membrane with $\lambda_1 = 2$, $\lambda_2 = 2.02$, and 0 kV electric excitation.

Figure 8(b) represents the FE and experimental frequencies of free vibration of a circular DE membrane having a radius of 0.05 m and initial thickness of 1 mm with $\lambda_1 = 2$, $\lambda_2 = 2.02$, and 0 kV electric excitation for the first three modes. The experimental research was conducted by Ojo et al. [18] by securing the tensed circular membrane within a rigid frame so that the fixed BC at the edge can be used similar to the experimental study conducted by Hays et al. [28]. From Figure 8(b), the frequencies obtained from the Ogden model assumption match closely again with the corresponding experimental frequencies. The maximum percent deviation between the experimental frequency and the Ogden model frequency is found to be 8.69% indicating that the computational frequencies are in reasonable agreement with the experimental frequencies.

3.2. Experimental Validation of the Fluid-Structure Interaction Model

A comparison between the aerodynamic coefficients obtained from the wind-tunnel experiment conducted by Pulok and Chakravarty [6] and a two-way, coupled FSI simulation for a circular membrane of radius 0.05 m with $\lambda_1 = 1.35$ and $\lambda_2 = 2.01$ for a Re of 91,367 without any applied voltage is depicted in Figure 9. Figure 9(a) compares the experimental coefficient of lift for the circular membrane to that obtained from the FSI simulation varying with the AoA. From Figure 9(a), a good agreement is observed between the experimental and simulated results where the maximum deviation was found as 10.8% for 15° AoA. Figure 9(b) on the other hand shows how the experimental coefficient of drag aligns with the simulated coefficient of drag leaving the maximum deviation of 7.69% for 10° AoA.

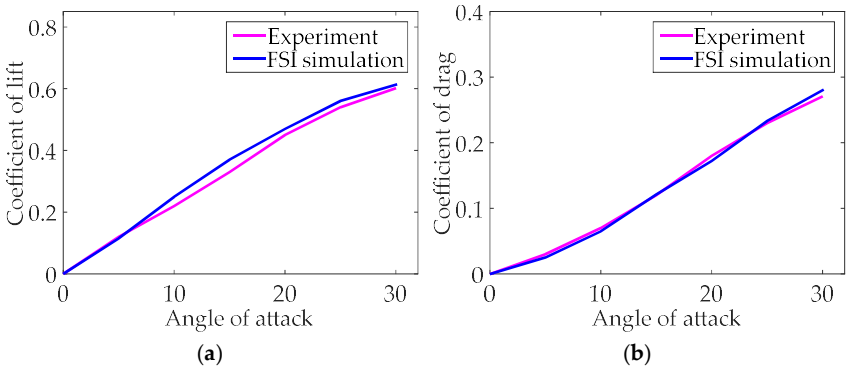

Figure 9. Variation of the **(a)** coefficient of lift; **(b)** coefficient of drag with angle of attack for a circular membrane having $\lambda_1 = 1.35$, $\lambda_2 = 2.01$, and 0 kV electric excitation obtained from experimental research and fluid-structure interaction simulation for a Re of 91,367.

It is to note that, for estimating the experimental coefficients of lift and drag, the total area considered by [6] in the corresponding analysis included both the membrane area and the area of the rigid ring in touch with the membrane near its edge. This might influence the deviation between the experimental and simulated coefficients of lift and drag because the steady lift and drag coefficients are also governed by the deformation of the membrane due to aerodynamic loading, also known as the aeroelastic deformation. In the experimental setup, part of the area of the membrane close to its boundary was securely attached to the rigid ring limiting its aeroelastic deformation around that part of the area, hereby affecting the experimental lift and drag coefficients accordingly. It is also to note that, for the coefficients of both lift and drag in the experimental research, the maximum AoA considered was 30° due to the limitation of the wind-tunnel setup used by Pulok and Chakravarty [6]. Moreover, in that experiment, the effect of relaxation on the membrane induced by the electric excitation was also not considered.

 doi:10.20944/preprints202603.1712.v1

4. Results and Discussion

4.1. Vibration Analysis

4.1.1. Mesh Convergence Study

To ensure that the computational results are reliable, a study of convergence for free vibration analysis of the membrane is performed to see how the results fluctuate with the increase of the solved numbers of DOFs associated with the increased number of mesh elements. Figure 10(a) indicates a variation of the natural frequency of free vibration for the rectangular DE membrane obtained from the FE analysis based on the Ogden model for $\lambda = 4.5$ for 4.5 kV with the number of DOFs. From Figure 10(a), the frequencies for the first three modes do not show that fluctuation with the increase in the number of DOFs and eventually, have been leveled indicating that the solutions have been converged.

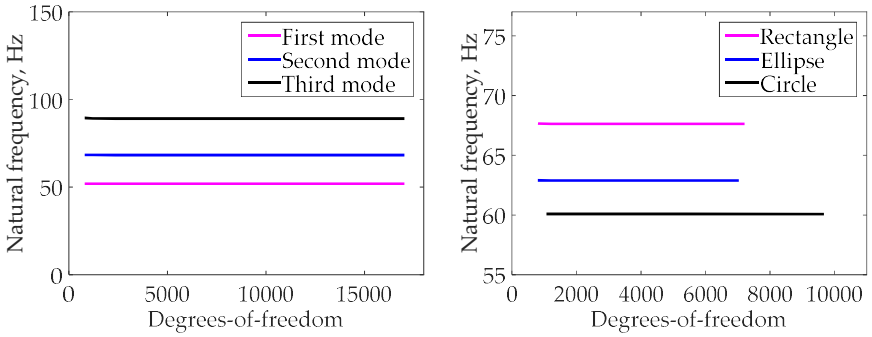

Figure 10. Variation of the natural frequencies with the numbers of degrees-of-freedom for **(a)** the rectangular membrane having a stretch ratio of 4.5 and an electric excitation of 4.5 kV for the first three modes; **(b)** for all the three shapes of the membranes having a stretch ratio of 3 and an electric excitation of 3.6 kV for the first mode.

Similar trend is found for Figure 10(b), where the variations of the fundamental frequencies (first mode frequencies) with increased numbers of DOFs for all the three shapes of the membranes are depicted for $\lambda = 3$ and an electric voltage of 3.6 kV. Thus, both Figures 10(a) and 10(b) show that the frequencies are converged for free vibration of the membranes of various shapes at different modes.

4.1.2. Natural Frequencies and Mode Shapes

Tables 7 and 8 represent the fundamental natural frequencies, i.e., frequencies for the first mode and frequencies of the subsequent three modes, respectively, for free vibration of all the three shapes of the membranes with λ ranging from 2 to 4.5 with different electric excitations obtained from the FE analysis. From both Tables 7 and 8, for a specific value of the stretch ratio, as the voltage increases, the natural frequency decreases. This is expected because with increasing applied voltage, the effect of relaxation becomes more dominating resulting in the decrease of the overall tension of the membrane, or in other words, reduced stiffness of the membrane, thus decreasing the frequencies. On the other hand, for a certain electric excitation, as the stretch ratio increases, the frequency of vibration also increases; since in that way the overall tension also increases as relaxation remains constant.

Table 7. Fundamental frequencies of free vibration of the membranes at different stretch ratios and electric excitations.

Mode	Frequency, Hz		
	$\lambda = 2$	$\lambda = 3$	$\lambda = 4.5$

 doi:10.20944/preprints202603.1712.v1

	0 kV			0 kV			0 kV		
	Rectangl	Ellips	Circl	Rectangl	Ellips	Circl	Rectangl	Ellips	Circle
1	51.05	47.47	45.36	77.12	71.71	68.52	115.76	107.64	102.8
	3.6 kV			3.6 kV			3.6 kV		
	Rectangl e	Ellips e	Circl e	Rectangl e	Ellips e	Circl e	Rectangl e	Ellips e	Circle
1	48.37	44.96	42.96	67.63	62.88	60.08	80.97	75.29	71.94
	4.5 kV			4.5 kV			4.5 kV		
	Rectangl e	Ellips e	Circl e	Rectangl e	Ellips e	Circl e	Rectangl e	Ellips e	Circle
1	46.79	43.49	41.55	61.72	57.36	54.81	51.98	48.33	46.18

Table 8. Second, third, and fourth mode frequencies of free vibration of the membranes at different stretch ratios and electric excitations.

	Frequency, Hz								
	$\lambda = 2$			$\lambda = 3$			$\lambda = 4.5$		
Mod	0 kV			0 kV			0 kV		
e	Rectangl	Ellips	Circle	Rectangl	Ellips	Circle	Rectangl	Ellips	Circle
2	67.08	67.13	72.27	101.35	101.41	109.1	152.11	152.21	163.8
3	87.50	83.11	96.86	132.19	125.55	146.3	198.41	188.44	219.6
4	92.37	87.96	104.1	139.54	132.88	157.2	209.44	199.44	236.0
	3.6 kV			3.6 kV			3.6 kV		
	Rectangl e	Ellips e	Circle	Rectangl e	Ellips e	Circle	Rectangl e	Ellips e	Circle
2	63.53	63.57	68.48	88.86	88.92	95.73	106.40	106.47	114.6
3	82.87	78.70	91.74	115.91	110.09	128.3	138.78	131.81	153.6
4	87.47	83.30	98.61	122.35	116.51	137.9	146.49	139.50	165.1
	4.5 kV			4.5 kV			4.5 kV		
	Rectangl e	Ellips e	Circle	Rectangl e	Ellips e	Circle	Rectangl e	Ellips e	Circle
2	61.45	61.50	66.21	81.06	81.11	87.33	68.30	68.35	73.59
3	80.16	76.14	88.74	105.74	100.42	117.0	89.10	84.62	98.63
4	84.62	80.58	95.39	111.61	106.29	125.8	94.05	89.56	106.0

However, an interesting phenomenon is observed for the fundamental frequencies listed in Table 7 where, for a specific prestretch and relaxation, the rectangular membrane demonstrates the highest frequency of vibration, and the circular membrane shows the lowest frequency. However, for higher modes, the frequencies mentioned in Table 8 show that the circular membrane provides higher values of frequencies compared to rectangular and elliptical membranes. Hence, it can be concluded that the rectangular membrane has a potential to remain stiffer in the lowest mode of vibration with broader scopes to delay the resonance and greater resistance to aeroelastic instability. The mode shapes for the first four modes of free vibration for all the three shapes of the membranes are depicted in Figure 11.

Rectangular membrane

 doi:10.20944/preprints202603.1712.v1

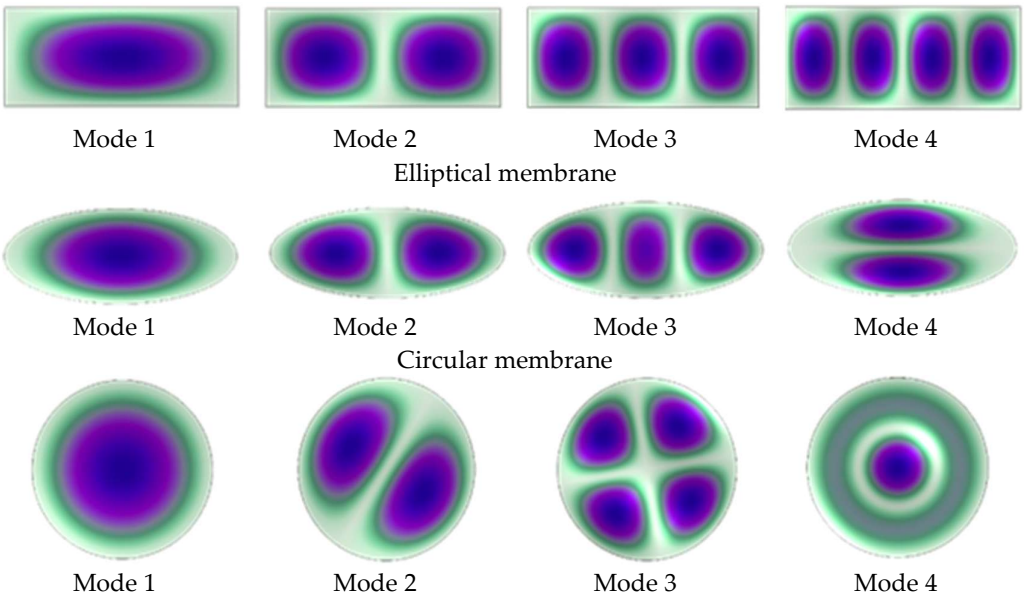

Figure 11. Mode shapes for the first four modes of free vibration for different shapes of membranes.

4.2. Aerodynamic Analysis

4.2.1. Effect of Prestretch

One of the important parameters that can regulate the dynamic characteristics of pliant membrane wings within its aerodynamic environment is the stretch ratio. The effect of prestretch on the coefficient of lift with varying AoA is explained in Figure 12(a) for a circular membrane subjected to an electric excitation of 4.5 kV and an airflow velocity of 13.4 m/s. Four different stretch ratios are considered to correlate the corresponding variations of the coefficient of lift with the AoA. From Figure 12(a), with constant relaxation induced by the 4.5 kV electric excitation for all the stretch ratios, the lift decreases as the stretch ratio increases. Similar characteristics are observed for the rectangular and the elliptical membranes as well. The reason behind this behavior can be attributed to the continuous reduction in membrane elasticity with the increase in the stretch. Two different physics to note here governing the mechanics of the membrane at the same time; one is the induced tensile stress on the membrane due to prestretch, and the other is the compressive stress created by the electric excitation. The combination of these stresses acting in opposite directions provides a net tension in the membrane. This net membrane tension increases with the increased values of prestretch, i.e., λ and with that, the membrane continues to lose its flexibility. From Figure 12(a), the notable difference in the coefficient of lift is observed once the stretch ratio reaches a value of 3 and higher and AoA approximates around 8° or higher. This behavior is identified as similar to the experimental study conducted by Maqsood and Go [8] for latex square membranes of various sizes for an air velocity of 15 m/s justifying that the effect of stretching can play a crucial role in altering the aerodynamic characteristics for pliant wings. In addition, it can be conjectured that a stretch ratio of 3 or higher can provide notable tension in the membrane after which significant change in aerodynamic characteristics in the membrane can be expected, and hence, $\lambda = 3$ or higher can be categorized as moderate to large stretch ratio.

 doi:10.20944/preprints202603.1712.v1

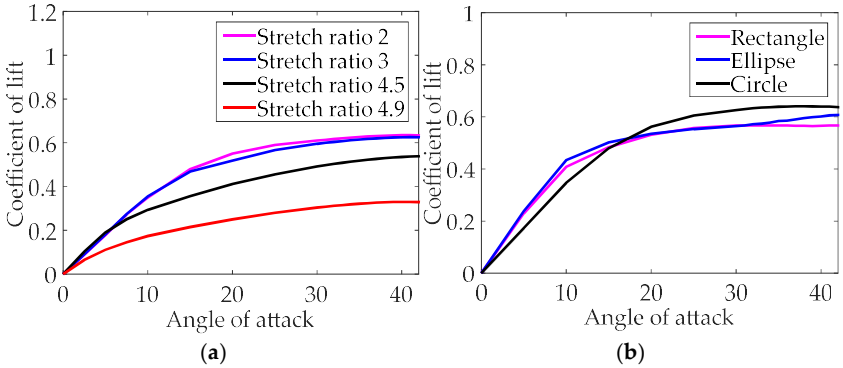

Figure 12. Variation of the coefficient of lift with angle of attack for (**a**) the circular membrane for air velocity of 13.4 m/s with 4.5 kV of electric excitation and stretch ratios 2, 3, 4.5, and 4.9; (**b**) three shapes of the membranes for an air velocity of 10 m/s with 0 kV electric excitation and stretch ratio 4.5.

Figure 12(b) signifies the effect of prestretch as well as the individual aerodynamic characteristics of the membranes of various shapes without any electric excitation for an air velocity of 10 m/s with a stretch ratio of 4.5. From Figure 12(b), the lift force for the circular membrane is associated approximately with a stall angle of 39°. However, that characteristic is different for the other two shapes of the membranes. For both rectangular and elliptical membranes, the stall is delayed to some extent unlike the circular membrane and is not apparent, thereby providing slightly more leeway to regulate the corresponding aerodynamic behaviors.

4.2.2. Effect of Relaxation

The effect of electric excitation on the tensed membrane is reflected in its relaxation which reduces the overall tension in the membrane. This is due to the compressive Maxwell stress along the thickness direction of the membrane resulting in an expansion of the membrane thereby reducing the overall tension. The higher the electric excitation for the membrane at a specific stretch ratio, the greater the relaxation is. Figure 13(a) presents the variation of the coefficient of lift with the AoA for the circular membrane for three different voltages, 0 kV, 3.6 kV, and 4.5 kV for a stretch ratio of 3 and an air flow velocity of 13.4 m/s. From Figure 13(a), the variation of the electric voltage does not reveal significant changes in the aerodynamic behavior of the membrane. However, if the stretch ratio is increased to 4.5 from 3, a significant change is observed in the aerodynamic performance as can be seen in Figure 13(b). From Figure 13(b), the 4.5 kV case provides slightly higher values of coefficient of lift until the AoA reaches 7° compared to 0 kV and 3.6 kV cases, and after that, decreased coefficient of lift is observed for the 4.5 kV case compared to the 0 kV and 3.6 kV cases. Before reaching the AoA of 7°, the 4.5 kV case shows approximately 25% increase in the coefficient of lift compared to the 0 kV case. The stall angles can be approximated as 40° for both the 0 kV and 3.6 kV cases, however, for the 4.5 kV case, the stall is not apparent or more precisely, it reflects a benign pattern in the vicinity of stall. This behavior is well aligned with the experimental study conducted by Maqsood and Go [8], where they estimated the coefficient of lift for a tensed square-shaped, Nylon membrane of dimensions 15 cm by 15 cm exposed to a flow velocity of 15 m/s subjected to a 1 cm relaxation.

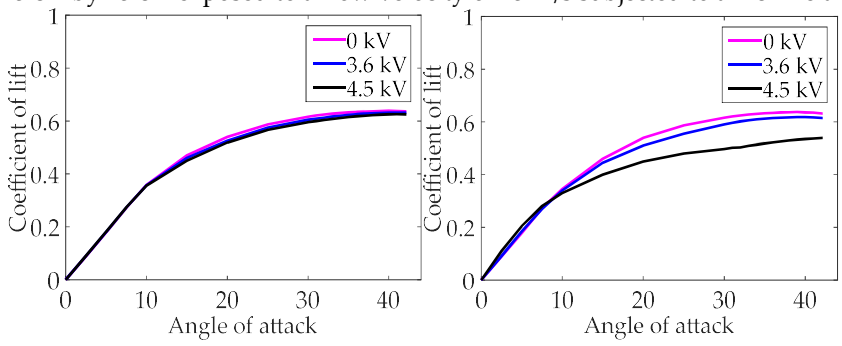

 doi:10.20944/preprints202603.1712.v1

(**a**) (**b**)

Figure 13. Variation of the coefficient of lift with angle of attack for the circular membrane with different electric excitations at a flow velocity of 13.4 m/s for **(a)** stretch ratio 3; **(b)** stretch ratio 4.5.

The behavior observed for the circular membrane under relaxation for a stretch ratio of 4.5 at 13.4 m/s with 0, 3.6, and 4.5 kV electric excitations is similarly observed for the rectangular and elliptical membranes. However, for the rectangular membrane, the increase in the coefficient of lift before 7° AoA for the 4.5 kV case is found to be 15% unlike the circular membrane, which is observed as 4% for the elliptical membrane at an AoA of approximately 15°. Thus, a summary can be concluded that the elliptical shape is more suitable to maintain the enhanced lift characteristics for a broader range of AoA compared to the rectangular and circular membranes.

The characteristic of the coefficient of drag for the circular membrane is described in Figures 14(a) and 14(b) for different voltages and 13.4 m/s flow velocity for $\lambda = 3$ and $\lambda = 4.5$, respectively. Similar to Figure 13(a), Figure 14(a) shows that the coefficient of drag does not vary significantly with change in voltages for $\lambda = 3$; however, for $\lambda = 4.5$, notable difference in the coefficient of drag is observed between 0 kV case and the 4.5 kV case. For $\lambda = 4.5$, the coefficient of drag shows higher values for the 4.5 kV case compared to the 0 kV case up to around 6° AoA; and after that the coefficient of drag for the 4.5 kV case shows a decrease for the remaining range of AoA. With increased relaxation for 4.5 kV, the circular membrane shows up to 16% increase in the coefficient of drag before 6° AoA.

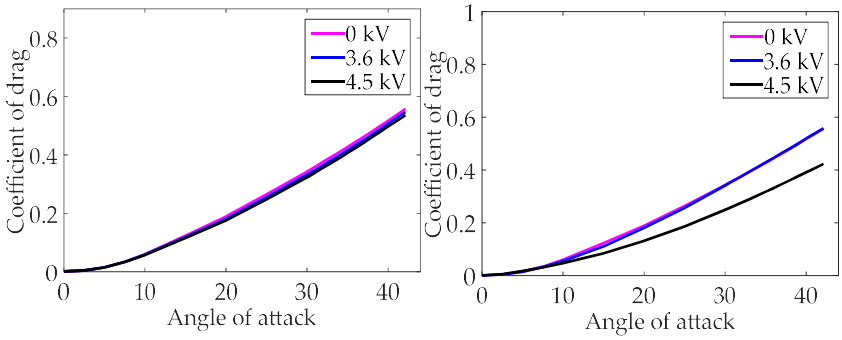

(**a**) (**b**)

Figure 14. Variation of coefficient of drag with angle of attack for the circular membrane with different electric excitations at a flow velocity of 13.4 m/s for **(a)** stretch ratio 3; **(b)** stretch ratio 4.5.

Similar trend of variation of the coefficient of drag with AoA for different electric excitations is found for the rectangular and the elliptical membranes. However, for the elliptical membrane, the coefficient of drag shows an increased value for the 4.5 kV case compared to the 3.6 kV case for the entire range of the AoA. This finding is very well aligned with the experimental results obtained by Hays et al. [28] for a VHB 4910 elliptical membrane having an initial thickness of 1 mm subjected to 3.6 kV electric excitation, air flow velocity of 10 m/s, and a stretch ratio of 3.

Table 9 shows the peak coefficients of lift and drag as well as the stall characteristics for all the three shapes of the membranes for an air velocity of 13.4 m/s subjected to the stretch ratio varying from 3 to 4.9 and electric excitation varying from 0 kV to 4.5 kV. Relaxation increases as the electric excitation for a specific stretch ratio increases from 0 kV to 4.5 kV from top to bottom of Table 9 affecting the stall characteristics. For the rectangular and elliptical membranes, the stall angle is not apparent for all three electric excitations for all stretch ratios; or in other words, it is delayed. Slightly different than that, the circular membrane shows an increasing trend of the stall angle with the increase of the electric excitation, and once the stretch ratio reaches 4.5 and higher, then with 4.5 kV excitation, the stall pattern shows the same trend as the rectangular and elliptical membranes. This indicates that a higher relaxation after a moderate stretch ratio can help provide a delayed stall for flexible membranes. These characteristics are well aligned with the experimental findings observed by Hays et al. [5,28] in their research as mentioned earlier.

 doi:10.20944/preprints202603.1712.v1

Table 9. Peak coefficient of lift, peak coefficient of drag, and stall characteristics at different stretch ratios and electric excitations for different shapes of the membranes subjected to an air velocity of 13.4 m/s (NA-Not apparent).

	0 kV								
	$\lambda = 3$			$\lambda = 4.5$			$\lambda = 4.9$		
Membrane	C_L	C_D	Stall	C_L	C_D	Stall	C_L	C_D	Stall
Rectangle	0.58	0.51	NA	0.58	0.51	NA	0.58	0.51	NA
Ellipse	0.61	0.53	NA	0.61	0.53	NA	0.62	0.54	NA
Circle	0.54	0.42	41°	0.64	0.55	40°	0.64	0.55	38°
	3.6 kV								
	$\lambda = 3$			$\lambda = 4.5$			$\lambda = 4.9$		
Membrane	C_L	C_D	Stall	C_L	C_D	Stall	C_L	C_D	Stall
Rectangle	0.58	0.51	NA	0.59	0.50	NA	0.59	0.49	NA
Ellipse	0.62	0.53	NA	0.61	0.51	NA	0.60	0.50	NA
Circle	0.63	0.54	41°	0.62	0.55	40°	0.60	0.50	40°
	4.5 kV								
	$\lambda = 3$			$\lambda = 4.5$			$\lambda = 4.9$		
Membrane	C_L	C_D	Stall	C_L	C_D	Stall	C_L	C_D	Stall
Rectangle	0.59	0.50	NA	0.57	0.40	NA	0.38	0.33	NA
Ellipse	0.62	0.52	NA	0.61	0.54	NA	0.35	0.33	NA
Circle	0.63	0.53	42°	0.54	0.42	NA	0.33	0.31	NA

In the analysis of Table 9 from left to right, an interesting phenomenon is observed. As the stretch ratio increases from 3 to 4.9 along the row, it is generally assumed that the membrane gets increasingly tensed. However, there is an optimum point depending on the applied relaxation after which even if the stretch ratio increases, the membrane gets increasingly relaxed. This is because, with the increase in relaxation due to higher electric voltage, the value of the second term on the right-hand side of Equations (3) and (4) also becomes higher for a certain stretch ratio which reduces the overall tension in the membrane. In Table 9, for all the membranes with λ ranging from 3 to 4.9, the 0 kV case provides increased tension in the membrane from left to right. However, for the 4.5 kV electric excitation with λ ranging from 3 to 4.9 from left to right of the table, decreased tension is noticed meaning increased relaxation. Hence, even though the stall angle is initially found as 42° for $\lambda = 3$ with 4.5 kV electric voltage for the circular membrane, eventually, the stall is delayed as λ increases from 3 because of having continued increase in relaxation. Thus, with higher relaxation for a certain stretch ratio, the rectangular and elliptical membranes can provide slightly more control to delay the stall; however, all the shapes behave identically if both the relaxation effect and stretch ratio are enhanced simultaneously.

4.2.3. Aerodynamic Efficiency

Although, for some specific applications, more lift force is desired for pliant wings operated within low-Re environments; usually, in majority of the cases, the aerodynamic efficiency [33] has relatively more importance than the lift force itself from the design point of view. For any flight, the lift force plays a critical role; however, enhancing the lift-to-drag ratio, alternatively known as aerodynamic efficiency, is the primary goal for efficient design of small-scale aerial structures composed of flexible wings. Hence, a comparison of the aerodynamic efficiency for all the shapes of

 doi:10.20944/preprints202603.1712.v1

the membranes for different air velocities, electric excitations, and stretch ratios are analyzed in the subsequent sections.

Figure 15 describes the variation of aerodynamic efficiency with AoA for the rectangular membrane with $\lambda = 3$ for three different air flow velocities where Figure 15(a) is for 0 kV electric excitation and Figure 15(b) is for 4.5 kV electric excitation. From both figures, the aerodynamic efficiency is enhanced significantly approximately until 11° AoA as the air flow velocity is increased, and the peak efficiency is recorded at an AoA of around 2.5°. Compared to Figure 15(a), Figure 15(b) shows that an increase to 4.5 kV electric voltage from 0 kV enhances the aerodynamic efficiency by around 4.3%. This trend is also observed by Hays et al. [5,28] in their experimental study of a stressed elliptical membrane of 1 mm initial thickness for $\lambda = 3$ for an airflow velocity of 10 m/s as the voltage increased from 0 kV to 3.6 kV. From the computational analysis, out of the three membrane shapes, the elliptical membrane is found to show the highest aerodynamic efficiency, and the circular membrane is observed to have the lowest aerodynamic efficiency for all the conditions used in Figure 15.

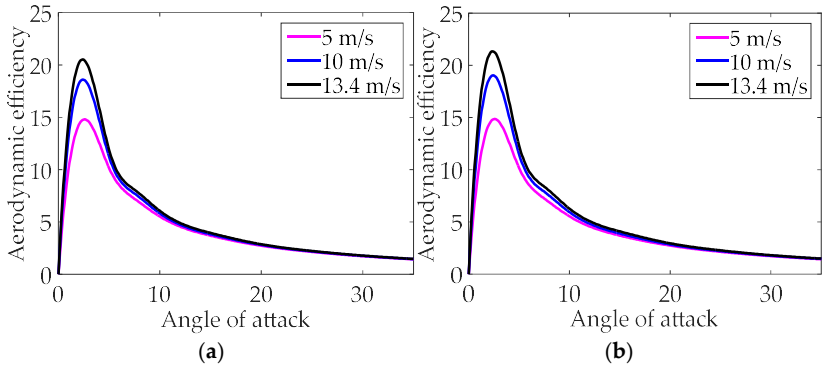

Figure 15. Variation of the aerodynamic efficiency of the rectangular membrane with the AoA at $\lambda = 3$ for 5 m/s, 10 m/s, and 13.4 m/s for **(a)** 0 kV; **(b)** 4.5 kV.

Instead of $\lambda = 3$, use of a higher stretch ratio, $\lambda = 4.5$ in Figure 16(a) reveals an interesting characteristic regarding the aerodynamic efficiency of the rectangular membrane for the three velocities with 4.5 kV electric excitation compared to Figure 15(b). Unlike Figure 15(b), a decreased peak aerodynamic efficiency near the AoA of 2.5° for 13.4 m/s air velocity is observed in Figure 16(a). This is because, for a 50% increase in λ from 3 to 4.5 with airflow velocity of 13.4 m/s, the peak lift coefficient is increased by around 12%, however, the drag is also enhanced by more than 28% reducing the overall aerodynamic efficiency compared to $\lambda = 3$. Although, with high stretch ratio, the tensile stress in the membrane increases; the compressive Maxwell stress εE^2 in Equations (3) and (4) at the same time also increases with increased voltage enhancing the relaxation and counterbalances a relatively large portion of the tensile stress in the membrane resulting in a lower overall membrane tension. Hence, the camber effect of the membrane due to aerodynamic loading at higher stretch ratio becomes more dominating resulting in more membrane deformation and forming a thicker shape of the membrane which ultimately creates larger drag and reduced aerodynamic efficiency. Compared to $\lambda = 3$, for $\lambda = 4.5$, the circular membrane is found to show the highest aerodynamic efficiency, and the rectangular membrane is found to show the lowest aerodynamic efficiency for the same electric excitation.

 doi:10.20944/preprints202603.1712.v1

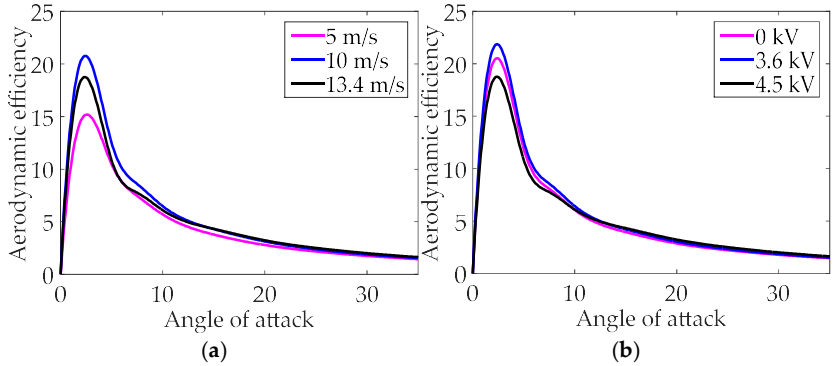

Figure 16. Variation of the aerodynamic efficiency of the rectangular membrane with the AoA at $\lambda = 4.5$ for **(a)** 5 m/s, 10 m/s, and 13.4 m/s for 4.5 kV; **(b)** 13.4 m/s for 0 kV, 3.6 kV, and 4.5 kV.

The aerodynamic efficiency varying with the AoA for the rectangular membrane for an air velocity of 13.4 m/s at $\lambda = 4.5$ is shown in Figure 16(b) for different electric excitations. From Figure 16(b), the peak aerodynamic efficiency corresponds to 3.6 kV compared to 0 kV and 4.5 kV. This indicates that the aerodynamic efficiency for a pliant membrane does not necessarily increase with higher relaxation within a low-Re environment. This phenomenon is characterized and reported by Hays et al. [5,28] in their experimental study of aerodynamic response of a VHB 4910 elliptical membrane for $\lambda = 3$ subjected to the same three electric excitations used in Figure 16(b) for a Re of 63,000 which justifies the simulated behavior of the flexible membranes in term of the aerodynamic efficiency under different electric excitations from moderate to higher stretch ratios.

Table 10 provides a summary of the percent change of the peak aerodynamic efficiency of different shapes of the membranes with change in electric excitations for different air flow velocities for stretch ratios 3 and 4.5. From Table 10, the circular membrane shows no negative percentage change in aerodynamic efficiency compared to the rectangular and elliptical membranes for both $\lambda = 3$ and $\lambda = 4.5$, indicating a tendency of offering an enhancement in aerodynamic efficiency with certain increase in electric voltage and air flow velocity. Similar behavior is found for the elliptical membrane for $\lambda = 3$; however, when the stretch ratio increases from 3 to 4.5, the percent change in peak aerodynamic efficiency shows a gradual reduction with change in electric excitations from 0 kV to 4.5 kV for all the air flow velocities. The rectangular membrane shows the highest decrease in aerodynamic efficiency for $\lambda = 4.5$ and air flow velocity of 13.4 m/s for a change in electric excitation from 0 kV to 4.5 kV. From Table 10, the circular membrane provides nearly steady change in aerodynamic efficiency with changes in electric excitation, velocity, and pretension and thus, can be considered as more suitable for achieving better aerodynamic performance within a specified range of pretension and relaxation.

Table 10. Percentage change in peak aerodynamic efficiency for different air flow velocities and stretch ratios for different shapes of the membranes with change in electric excitations.

Change in peak aerodynamic efficiency (%)							
		$V = 5$ m/s		$V = 10$ m/s		$V = 13.4$ m/s	
		0–3.6 kV	0–4.5 kV	0–3.6 kV	0–4.5 kV	0–3.6 kV	0–4.5 kV
$\lambda = 3$	Rectangle	0.20	0.41	1.23	2.31	2.24	4.00
	Ellipse	0.26	0.52	1.53	2.84	1.76	4.81
	Circle	0.21	0.42	1.19	2.25	2.20	4.05
$\lambda = 4.5$	Rectangle	0.74	2.63	4.20	11.67	6.54	-9.40
	Ellipse	0.91	-0.46	5.21	-2.70	8.28	-4.86

 doi:10.20944/preprints202603.1712.v1

	Circle	0.99	3.17	4.18	13.38	6.97	5.48

4.2.4. Aeroelastic Analysis

The aeroelastic behavior of three shapes of the DE membranes is investigated for different air flow velocities and electric excitations. Table 11 shows the aeroelastic characteristics of the membranes in terms of the peak out-of-plane deformations for different air flow velocities and electric excitations for a stretch ratio of 3. From Table 11, as expected, with the increase in relaxation for a certain air flow velocity, the peak deformation of the membrane increases. This is because, with higher voltage or increased relaxation, the overall tension in the membrane is reduced, making the membrane increasingly flexible. The deformation becomes higher with increased air flow velocity because of the enhanced lift force due to increased velocity. From Table 11, it is apparent that the rectangular membrane is subjected to the least deformation and the circular membrane undergoes the largest deformation for a certain air flow velocity and relaxation. From this analysis, the circular membrane is observed to have more potential to change its shape under aerodynamic loading due to its increased flexibility and thus, can have more impact in altering the flow field and/or affecting the passive flow control. Figure 17 shows the contour plots of out-of-plane deformations for all the membranes for an air flow velocity of 13.4 m/s, 40° AoA, and for $\lambda = 3$ with an electric excitation of 4.5 kV showing that the peak out-of-plane deformation occurs near the center for all the shapes of the membranes.

Table 11. Maximum out-of-plane deformation for different shapes of the membranes with different electric excitations and air velocities at a stretch ratio of 3.

Maximum out-of-plane deformation, mm									
	$\lambda = 3$								
V, m/s	0 kV			3.6 kV			4.5 kV		
	Rectangle	Ellipse	Circle	Rectangle	Ellipse	Circle	Rectangle	Ellipse	Circle
5	0.45	0.60	0.66	0.60	0.75	0.86	0.72	0.91	1.04
10	1.86	2.34	2.70	2.45	3.05	3.49	2.95	3.66	4.16
13.4	3.35	4.21	4.74	4.40	4.97	6.01	5.24	6.37	7.04

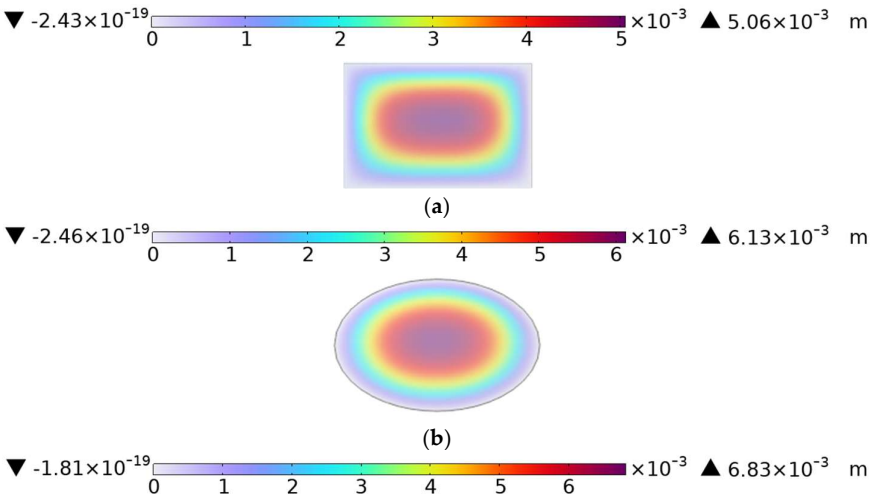

 doi:10.20944/preprints202603.1712.v1

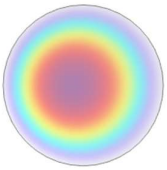

(c)

Figure 17. Contour plot of out-of-plane deformation of the **(a)** rectangular; **(b)** elliptical; **(c)** circular membrane, for a stretch ratio of 3, 4.5 kV electric voltage, 40° AoA, and 13.4 m/s air flow velocity.

5. Conclusions

In this research, the structural dynamic and aerodynamic characteristics of the VHB 4910 membrane of three different geometric shapes with same surface areas are computationally investigated for different air flow velocities, stretch ratios, and electric excitations. For the structural dynamic analysis, a computational finite element model is developed to estimate the natural frequencies of vibration using the Ogden hyperelastic model approximation. Following that, for the aerodynamic analysis, a two-way, fully coupled computational fluid-structure interaction model is developed to analyze the effect of stretch ratios, relaxation, aerodynamic efficiency, and elastic deformation. The simulation results are compared with experimental results published in literature for validating the computational models. The following conclusions can be drawn from this research:

1. The Ogden hyperelastic model captures the natural frequency of free vibration of all shapes of the membranes in a consistent manner for various pretensions and relaxations. The rectangular membrane shows higher frequency in the fundamental mode of vibration offering more leeway to delay the resonance and has a potential to offer greater resistance to aeroelastic instability. This characteristic is observed in the circular membrane in higher modes.

2. A stretch ratio of three or higher can generally be defined as a moderate stretch ratio in the perspective of this research as significant changes in structural and aerodynamic characteristics are observed at or above a stretch ratio of three.

3. Increased relaxation applied to a flexible membrane for a stretch ratio higher than the moderate range can enhance the coefficient of lift up to a narrow range of angle of attack, however, provides decreased coefficient of lift after that.

4. An elliptical membrane offers a broader range of angle of attack compared to the rectangular and circular shapes of membranes within which enhanced lift coefficients are observed for increased relaxation. However, an increased coefficient of drag is also found for the elliptical membrane for higher relaxation compared to other shapes of the wings.

5. The rectangular and elliptical membranes provide a little more flexibility to regulate the stall compared to the circular membrane with higher relaxation at a certain stretch ratio.

6. For moderate stretch ratio ($\lambda \approx 3$) with different velocities and increased relaxation, the elliptical membrane shows the highest aerodynamic efficiency. However, when the stretch ratio increases beyond this moderate level ($\lambda > 3$), the circular membrane exhibits superior aerodynamic efficiency compared to the rectangular and elliptical membranes. Also, the circular membrane is found to provide better aerodynamic performance within a certain range of electric excitation and pretension.

7. The circular membrane can have more influence in altering the flow field and/or affecting the passive flow control due to its more flexibility in changing its shape.

Author Contributions: Conceptualization, P.S.; methodology, P.S. and B.F.; software, P.S. and B.F.; validation, P.S. and B.F.; formal analysis, P.S. B.F., and M.R.; investigation, P.S. and B.F.; resources, P.S.; data curation, P.S. and B.F.; writing–original draft preparation, P.S., B.F., and M.R.; writing–review and editing, P.S., B.F., and M.R.; visualization, P.S. and M.R.; supervision, P.S.; project administration, P.S.; funding acquisition, P.S. All authors have read and agreed to the published version of the manuscript.

 doi:10.20944/preprints202603.1712.v1

Funding: This research was partially supported by the funding through Embry-Riddle Aeronautical University's Faculty Research Development Program (FRDP), Faculty Innovative Research in Science and Technology (FIRST) Program, and Undergraduate Research Institute (URI).

Data Availability Statement: The data presented in this study are available on request from the corresponding author, as certain simulation modules are part of ongoing research and are not yet suitable for public dissemination.

Acknowledgments: The authors acknowledge the financial and technical support from the Embry-Riddle Aeronautical University to accomplish the study.

Conflicts of Interest: The authors declare no conflicts of interest. The funders had no role in the design of the study; in the collection, analyses, or interpretation of data; in the writing of the manuscript; or in the decision to publish the results.

Nomenclature

The following symbols are used in this manuscript:

C_L	lift coefficient
C_D	Drag coefficient
E	true electric field
L_c	chord length of the membrane aligned parallel to the airflow velocity
N	number of terms to be used in the hyperelastic model
P	pressure
V	air flow velocity
W	strain energy density function
$\mathbf{a_s}$	acceleration vector
d	distance between the neutral axis and centroidal axis
$d_x,\ d_y,\ d_z$	linear displacement along X axis, Y axis, Z axis
f	natural frequency in Hz
$\mathbf{f_s}$	force vector per unit volume
$g_x,\ g_y,\ g_z$	acceleration due to gravity along X axis, Y axis, Z axis
i	Index representing integer
t	time
t_u	thickness of the membrane in the undeformed state
$u,\ v,\ w$	velocity component along X axis, Y axis, Z axis
$x,\ y,\ z$	independent displacement variables along X axis, Y axis, Z axis
α_i	material constant for hyperelastic model
α_a	angle of attack
ε	permittivity
$\theta_x,\ \theta_y,\ \theta_z$	angular displacement about X axis, Y axis, Z axis
λ	stretch ratio
μ_i	material constant for hyperelastic model
μ_s	shear modulus of dielectric elastomer
μ_d	dynamic viscosity of air
$\rho_a,\ \rho_m$	density of air, membrane
$\sigma_x,\ \sigma_y$	stress on the membrane along X axis, Y axis
$\boldsymbol{\sigma_s}$	stress tensor

References

1. Hajiesmaili, E. and D.R. Clarke, *Dielectric elastomer actuators.* Journal of Applied Physics, 2021. **129**(15).

 doi:10.20944/preprints202603.1712.v1

2. Zhang, Q., et al., *A Review of the Applications and Challenges of Dielectric Elastomer Actuators in Soft Robotics.* Machines, 2025. **13**(2): p. 101.
3. Lu, T., C. Ma, and T. Wang, *Mechanics of dielectric elastomer structures: A review.* Extreme Mechanics Letters, 2020. **38**: p. 100752.
4. Cooley, C.G. and R.L. Lowe, *Nonlinear vibration of dielectric elastomer membranes with axial inertia effects.* International Journal of Mechanical Sciences, 2023. **248**: p. 108205.
5. Hays, M.R., et al., *Aerodynamic control of micro air vehicle wings using electroactive membranes.* Journal of Intelligent Material Systems and Structures, 2013. **24**(7): p. 862-878.
6. Pulok, M.K.H. and U.K. Chakravarty, *Modal Characterization, Aerodynamics, and Gust Response of an Electroactive Membrane.* AIAA Journal, 2022. **60**(5): p. 3194-3205.
7. Zhu, J., S. Cai, and Z. Suo, *Resonant behavior of a membrane of a dielectric elastomer.* International Journal of Solids and Structures, 2010. **47**(24): p. 3254-3262.
8. Maqsood, A. and T.H. Go, *Aerodynamic characteristics of a flexible membrane micro air vehicle.* Aircraft Engineering and Aerospace Technology, 2015. **87**(1): p. 30-37.
9. Kang, W., et al., *Modal Phase Study on Lift Enhancement of a Locally Flexible Membrane Airfoil Using Dynamic Mode Decomposition.* Aerospace, 2025. **12**(4): p. 313.
10. Lang, X., et al., *Effect of Wing Membrane Material on the Aerodynamic Performance of Flexible Flapping Wing.* Applied Sciences, 2022. **12**(9): p. 4501.
11. Zhao, D., et al., *Vibration study of dielectric elastomer conical structure based on fractional viscoelasticity.* Scientific Reports, 2025. **15**(1): p. 11445.
12. Gu, G. and Z. Lai, *Finite element analysis of dielectric elastomer membranes using shell elements.* Journal of Renewable and Sustainable Energy, 2018. **10**(4).
13. Kossa, A., M.T. Valentine, and R.M. McMeeking, *Analysis of the compressible, isotropic, neo-Hookean hyperelastic model.* Meccanica, 2023. **58**(1): p. 217-232.
14. Mihai, L.A., et al., *A comparison of hyperelastic constitutive models applicable to brain and fat tissues.* Journal of The Royal Society Interface, 2015. **12**(110): p. 20150486.
15. Liang, H., et al., *Characterizing the dielectric elastomer's complete mechanical behavior through an electromechanical coupling method.* Extreme Mechanics Letters, 2024. **71**: p. 102204.
16. Park, S.-Y., et al., *Hyperelastic and Stacked Ensemble-Driven Predictive Modeling of PEMFC Gaskets Under Thermal and Chemical Aging.* Materials, 2024. **17**(22): p. 5675.
17. Simón-Portillo, F.J., et al., *Methodology for the mechanical characterisation of hyperelastic adhesives. Experimental validation on joints of different thicknesses.* Polymer Testing, 2023. **129**: p. 108286.
18. Ojo, O., et al. *An Investigation on the Aerodynamics, Vibrations, and Control of an Electroactive Membrane*. in *ASME 2022 International Mechanical Engineering Congress and Exposition*. 2022.
19. Hu, S., W. Kang, and Y. Wang. *Fluid-structural interaction of dielectric elastic membrane airfoil*. in *2023 2nd International Symposium on Aerospace Engineering and Systems (ISAES)*. 2023.
20. Lin, Z.-h., et al., *Fluid-Structure Interaction Analysis on Membrane Behavior of a Microfluidic Passive Valve.* Membranes, 2020. **10**(10): p. 300.
21. Genç, M.S., et al., *Experimental analysis of fluid-structure interaction in flexible wings at low Reynolds number flows.* Aircraft Engineering and Aerospace Technology, 2021. **93**(6): p. 1060-1075.
22. Liang, C., et al., *Vibration Characteristic Analysis of Hollow Fiber Membrane for Air Dehumidification Using Fluid-Structure Interaction.* Membranes, 2023. **13**(2): p. 233.
23. Li, G., et al., *Aeroelastic characteristics of flexible membrane wings with ceiling effect.* Physics of Fluids, 2024. **36**(3).
24. Tong, X., et al., *Study on the Aeroelastic Characteristics of a Large-Span Joined-Wing Solar-Powered UAV.* Aerospace, 2025. **12**(10): p. 892.
25. Yeh, S.-I. and C.-H. Chiang, *The Influence of Wing Membrane Elasticity on Aerodynamics in a Bat-Inspired Flapping Robot.* Biomimetics, 2025. **10**(3): p. 161.
26. Sahu, R.K., et al., *Estimation and validation of maxwell stress of planar dielectric elastomer actuators.* Journal of Mechanical Science and Technology, 2016. **30**(1): p. 429-436.

 doi:10.20944/preprints202603.1712.v1

27. Dong, L., et al., *Resonant frequency tuning of electroactive polymer membranes* via *an applied bias voltage*. Smart Materials and Structures, 2018. **27**(11): p. 114005.
28. Hays, M.R., et al., *Fluid–structural dynamic characterization of an electroactive membrane wing*. Journal of Intelligent Material Systems and Structures, 2016. **27**(11): p. 1510-1522.
29. Gao, Z., A. Tuncer, and A.M. Cuitiño, *Modeling and simulation of the coupled mechanical–electrical response of soft solids.* International Journal of Plasticity, 2011. **27**(10): p. 1459-1470.
30. Rozov, V., et al. *CFD-Based Aeroelastic Sensitivity Study of a Low-Speed Flutter Demonstrator*. Aerospace, 2019. **6**, DOI: 10.3390/aerospace6030030.
31. Lampropoulos, N.K., et al., *Aerodynamic Performance of a Natural Laminar Flow Swept-Back Wing for Low-Speed UAVs Under Take Off/Landing Flight Conditions and Atmospheric Turbulence.* Aerospace, 2025. **12**(10): p. 934.
32. Anderson, D., Tannehill, J.C., & Pletcher, R.H., *Computational Fluid Mechanics and Heat Transfer*. 3 ed. 2013: CRC Press.
33. Kretov, A. and D. Tiniakov, *Evaluation of the Mass and Aerodynamic Efficiency of a High Aspect Ratio Wing for Prospective Passenger Aircraft.* Aerospace, 2022. **9**(9): p. 497.